

Article

Performance Comparison between AB₅ and Superlattice Metal Hydride Alloys in Sealed Cells

John M. Koch ¹, Kwo-Hsiung Young ^{1,2,*} , Jean Nei ¹ , Chaolan Hu ¹ and Benjamin Reichman ¹

¹ BASF/Battery Materials—Ovonic, 2983 Waterview Drive, Rochester Hills, MI 48309, USA;
john.m.koch@basf.com (J.M.K.); jean.nei@basf.com (J.N.); sherry.hu@basf.com (C.H.);
Benjamin.reichman@basf.com (B.R.)

² Department of Chemical Engineering and Materials Science, Wayne State University, Detroit, MI 48202, USA

* Correspondence: kwo.young@basf.com; Tel.: +1-248-293-7000

Academic Editor: Sheng S. Zhang

Received: 27 September 2017; Accepted: 17 October 2017; Published: 6 November 2017

Abstract: High-power cylindrical nickel metal/hydride batteries using a misch metal-based Al-free superlattice alloy with a composition of La_{11.3}Pr_{1.7}Nd_{5.1}Mg_{4.5}Ni_{63.6}Co_{13.6}Zr_{0.2} were fabricated and evaluated against those using a standard AB₅ metal hydride alloy. At room temperature, cells made with the superlattice alloy showed a 40% lower internal resistance and a 59% lower surface charge-transfer resistance compared to cells made with the AB₅ alloy. At a low temperature (−10 °C), cells made with the superlattice alloy demonstrated an 18% lower internal resistance and a 60% lower surface charge-transfer resistance compared to cells made with the AB₅ alloy. Cells made with the superlattice alloy exhibited a better charge retention at −10 °C. A cycle life comparison in a regular cell configuration indicated that the Al-free superlattice alloy contributes to a shorter cycle life as a result of the pulverization from the lattice expansion of the main phase.

Keywords: metal hydride (MH); nickel/metal hydride (Ni/MH) battery; hydrogen-absorbing alloy; electrochemistry; superlattice alloy

1. Introduction

Nickel/metal hydride (Ni/MH) batteries have been serving consumer portable electronics, hybrid electric vehicles, and stationary applications for more than 30 years [1–6]. Until now, the misch metal (Mm)-based AB₅ metal hydride (MH) alloy was the mainstream negative electrode active material [7]. In the last decade, the Mm-based superlattice MH alloy began to take over the market share because of its higher capacities; better high-rate dischargeability; and superior low-temperature, high-temperature, and charge retention performances compared to the conventional AB₅ MH alloy [2–6,8]. The superlattice MH alloy is composed of more than one phase with alternating A₂B₄ and AB₅ building slabs along the *c*-direction of the unit cell [2]. There can be one (AB₃), two (A₂B₇), three (A₅B₁₉), or more AB₅ units between two A₂B₄ slabs. Depending on the stacking sequence, either the hexagonal or rhombohedral structures are possible. The A-site of the superlattice MH alloy contains both rare-earth (RE) and alkaline earth (usually Mg) elements. While almost all academic research has focused on the single RE element (La or Nd)-based superlattice MH alloys (for reviews, see [9–11]), commercial applications have adopted the Mm composition for a higher cycle stability [2,12]. In the past, a few papers about the substitution works performed in the Mm-based superlattice alloy family with Al [13], Mn [14,15], Fe [16,17], Co [18–20], and Ce [21] were published, but a systematic performance comparison between a Mm-based superlattice MH alloy and a standard AB₅ MH alloy is absent. Therefore, we conducted a series of battery performance evaluations in the sealed cells made with both materials and report the results here.

2. Experimental Setup

Both the AB₅ and superlattice alloys were prepared by Eutectix (Troy, Michigan, USA) with a conventional 250 kg induction melting furnace [22]. The ingot was placed in a retort and annealed at 960 °C in vacuum (AB₅) or 1 atm atmosphere of Ar (superlattice) for 8 h. The annealed ingots were crushed and ground into the size of –200 mesh. A Philips X'Pert Pro X-ray diffractometer (XRD; Amsterdam, the Netherlands) and a JEOL-JSM6320F scanning electron microscope (SEM; Tokyo, Japan) were used to study the alloys' microstructures. A Suzuki Shokan multi-channel pressure–concentration–temperature system (PCT; Tokyo, Japan) was used to study the gaseous-phase hydrogen storage characteristics. Electrochemical properties were evaluated with negative electrodes made by dry compacting the annealed alloy powder onto an expanded nickel substrate. A CTE MCL2 Mini cell testing system (Chen Tech Electric MFG. Co., Ltd., New Taipei, Taiwan) was used to study the alloys' half-cell characteristics.

For the sealed-cell performance evaluation, a C-size cylindrical high-power design was chosen. Negative (0.193 mm thick) and positive electrodes (two thicknesses: 0.300 and 0.361 mm) were made using the dry-compaction and wet-paste methods [23], respectively. Positive electrode paste was composed of 89% standard AP50 [24] with a composition of Ni_{0.91}Co_{0.045}Zn_{0.045}(OH)₂ (BASF—Ovonic, Rochester Hills, Michigan, USA), and 5 wt % Co and 6% Co(OH)₂ powders on a nickel foam substrate. A Freudenberg FS2225 fluorinated acrylic acid grafted polyethylene/polypropylene non-woven fabric (Freudenberg Group, Weinheim, Germany) was used as the separator. In this high-power cell design, a high negative-to-positive capacity ratio cell design (about 1.7) was used to ensure a large amount of overcharge reservoir [25]. A 30 wt % KOH solution with LiOH (1.5 wt %) additive was used as the electrolyte. A six-cycle activation process using a Maccor battery cycler (Maccor, Tulsa, Oklahoma, USA) was conducted for each cell [26]. The battery performance testing procedures can be found in an earlier publication [27].

3. Results and Discussion

3.1. Alloy Properties Comparison

Alloy A, the most popular AB₅ alloy used in the industry with a composition of La_{10.5}Ce_{4.3}Pr_{0.5}Nd_{1.4}Ni₆₀Co_{12.7}Mn_{5.9}Al_{4.7}, was used as the control in this comparison work. Alloy B with a composition of La_{11.3}Pr_{1.7}Nd_{5.1}Mg_{4.5}Ni_{63.6}Co_{13.6}Zr_{0.2}, which shows the lowest charge-transfer resistance in a comparative study [28], was the superlattice alloy under the current study. In this composition, Pr and Nd were added to reduce the corrosion nature of the alloy, Ce and Mn were not included in the consideration of cycle stability and self-discharge [2,21], Co was added for low-temperature performance enhancement [19], and a very small amount of Zr was added for scavenging residual oxygen in the chamber. The B/A stoichiometry of 3.42 was chosen through an optimization study judging the electrochemical performance. While annealed alloy A has only one CaCu₅ phase, as seen from its XRD pattern (Figure 10a in [28]), alloy B shows a multi-phase structure in both pristine and annealed conditions (Figure 1). Phase abundances calculated from the XRD data are listed in Table 1. After annealing, the abundance of the desirable Nd₂Ni₇ phase [29] increased from 0 to 56.7 wt %; the unwanted CaCu₅ phase [30] decreased from 32.7 to 1.6 wt %; and LaMgNi₄ and other superlattice phases, such as CeNi₃, NdNi₃, Sm₅Ni₁₉ and Ni₅Co₁₉, still existed. SEM analysis was used to confirm the XRD findings, and two representative backscattering electron micrographs for pristine and annealed alloy B are shown in Figure 2. X-ray energy-dispersive spectroscopy (EDS) was used to study the chemical compositions of a few spots in Figure 2, and the results are summarized in Table 2. In the pristine sample, the AB₅ phase (spots 2 and 3) can be identified by its relatively bright contrast due to the higher content of low-atomic weight nickel. Later, the AB₅ phase was removed by annealing. The superlattice phases are difficult to separate by contrast in the micrographs because of their similar chemical composition and stoichiometry. The microstructural analyses conclude

that while annealed alloy A has only one CaCu₅ structure, alloy B (before or after annealing) is a superlattice-based (>95 wt %) multi-phase alloy.

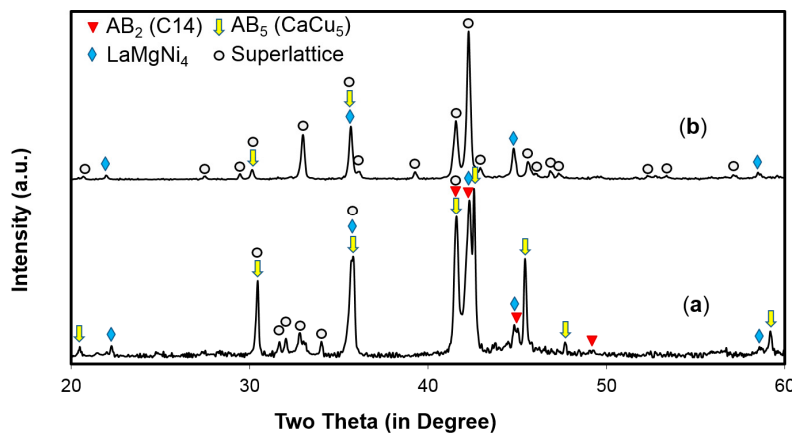


Figure 1. X-ray diffractometer (XRD) patterns using Cu-K α as the radiation source for (a) pristine, and (b) annealed alloy B.

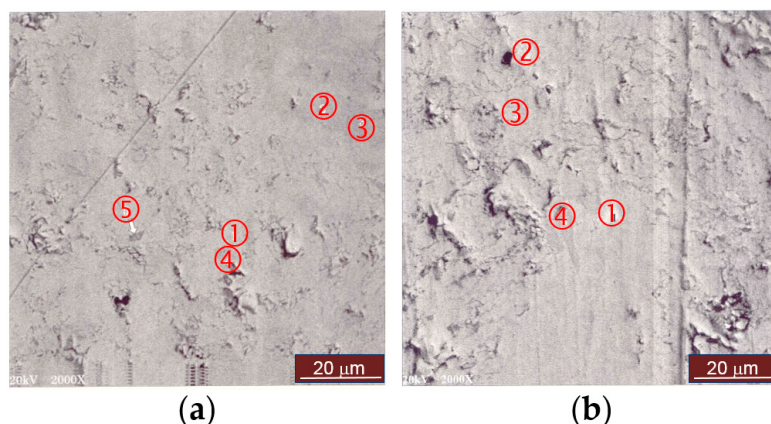


Figure 2. Scanning electron microscope (SEM) backscattering electron micrographs of (a) pristine, and (b) annealed alloy B.

Table 1. Phase abundances (in wt %) of alloy B before and after annealing determined by the X-ray diffractometer (XRD) analysis. HEX, CUB, and RHO are hexagonal, cubic, and rhombohedral, respectively.

Stoichiometry	AB ₂		AB ₃		A ₂ B ₇		A ₅ B ₁₉		AB ₅
Structure	HEX	CUB	HEX	RHO	HEX	RHO	HEX	RHO	HEX
Phase	MgZn ₂	LaMgNi ₄	CeNi ₃	NdNi ₃	Nd ₂ Ni ₇	Pr ₂ Ni ₇	Sm ₅ Ni ₁₉	Nd ₅ Co ₁₉	CaCu ₅
Pristine alloy B	7.9	5.7	2.0	19.3	0.0	13.1	1.6	17.7	32.7
Annealed alloy B	0.0	3.2	7.5	7.4	56.9	0.0	6.4	17.0	1.6

Both the gaseous phase and electrochemical hydrogen storage characteristics of alloys A (AB₅) and B (superlattice) were studied. In the gaseous phase, PCT isotherms measured at 30 °C for both alloys are plotted in Figure 3. Annealed alloy A has a higher plateau pressure and a higher reversible capacity than pristine and annealed alloy B. Annealing in alloy B flattens the isotherm, increases the storage capacity, and reduces the hysteresis, as reported previously [31]. Electrochemical testing results from the first 20 cycles of annealed alloys A and B are compared in Figure 4. Annealed alloy B exhibits a higher initial capacity, but it degrades quickly in the flooded KOH solution compared to annealed

Alloy A. The higher oxidation rate in the Mg-containing superlattice alloys is well known, and many electrode fabrication methods have been proposed to overcome this shortcoming [32]. As a result, a commercial cell capable of 6000 cycles with a superlattice alloy has been demonstrated [8]. Gaseous phase and electrochemical hydrogen storage properties of annealed alloys A and B are summarized in Table 3. Plateau pressure is defined as the equilibrium pressure corresponding to a 0.75 wt % storage capacity in the desorption isotherm, and the PCT hysteresis is defined as \ln (absorption pressure/desorption pressure) at the same storage capacity. Although the gaseous phase capacities of the two alloys are similar, the superlattice alloy shows a higher electrochemical discharge capacity, which is close to the theoretical limit converted from the gaseous phase capacity ($381 \text{ mAh}\cdot\text{g}^{-1}$ using the conversion of 1 wt % = $268 \text{ mAh}\cdot\text{g}^{-1}$) because of the synergetic effect among the constituent phases [33]. The higher PCT hysteresis in annealed alloy B predicts a higher pulverization rate during repetitive cycling [34].

Table 2. Energy-dispersive spectroscopy (EDS) results from selected spots in Figure 2. All numbers are percentages.

Location	La	Pr	Nd	Mg	Ni	Co	Zr	B/A	Phase
Figure 2a-1	13.6	0.7	4.5	6.6	62.6	11.9	0.1	2.93	Superlattice
Figure 2a-2	11.1	1.2	5.3	0.9	67.2	14.1	0.2	4.41	AB ₅
Figure 2a-3	9.5	0.9	5.6	0.4	69.1	14.4	0.1	5.10	AB ₅
Figure 2a-4	11.1	0.8	5.2	18.7	57.5	6.5	0.2	1.79	LaMgNi ₄
Figure 2a-5	5.5	0.4	3.5	0.0	17.8	3.2	69.6	9.64	ZrO ₂
Figure 2b-1	86.0	0.0	4.5	0.8	6.4	0.8	1.5	0.1	La metal
Figure 2b-2	16.3	0.7	4.1	4.0	61.5	13.2	0.2	2.98	Superlattice
Figure 2b-3	14.4	0.9	4.4	12.4	60.3	7.5	0.1	2.11	LaMgNi ₄
Figure 2b-4	13.2	0.7	4.7	14.2	60.4	6.7	0.1	2.04	LaMgNi ₄

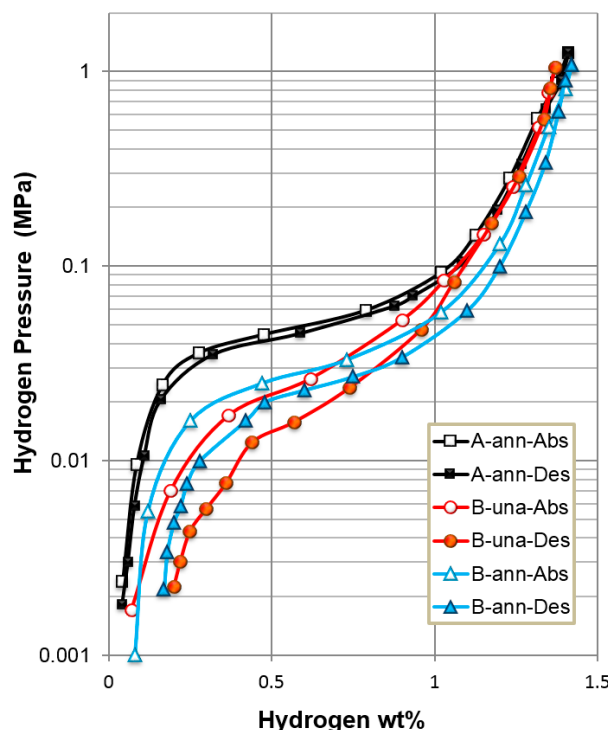


Figure 3. Pressure–concentration–temperature (PCT) isotherms measured at 30°C . A-ann, B-una, and B-ann are annealed alloy A, pristine alloy B, and annealed alloy B, respectively. Abs and Des denote absorption and desorption, respectively.

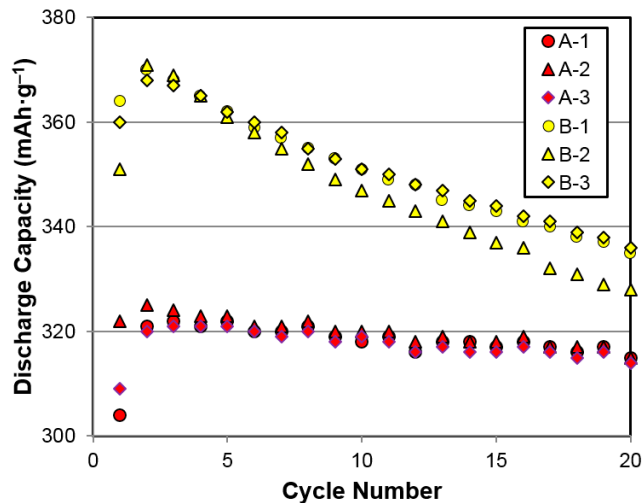


Figure 4. Half-cell capacities measured using the three-electrode cell setup for annealed alloys A and B.

Table 3. Gaseous phase and electrochemical hydrogen storage properties of annealed alloys A and B.

Alloy	Full H-Storage	Reversible H-Storage	Plateau Pressure	PCT Hysteresis	Discharge Capacity
Annealed alloy A	1.41%	1.37%	0.058 MPa	0.10	310 mAh·g ⁻¹
Annealed alloy B	1.42%	1.25%	0.025 MPa	0.23	370 mAh·g ⁻¹

3.2. Sealed-Cell Performance

Fifty C-size cylindrical cells in a high-power design were made with annealed alloys A (cell A) and B (cell B). After the formation process, the discharge capacities were 2.7 and 3.1 Ah from cells A and B, respectively, with a 0.6 A discharge current. Cell B shows a higher energy density ($50.4 \text{ vs } 41.0 \text{ Wh}\cdot\text{kg}^{-1}$) than cell A because of its higher active material capacity, which allows for the matching with a thicker positive electrode (0.361 vs 0.300 mm).

3.2.1. High-Rate

Room temperature (RT) discharge voltage profiles with four different rates (C, 2C, 5C, and 10C) for cells A and B are shown in Figure 5. The cell voltage (V) decreases with the increase in the discharge current (i) following the formula:

$$V = V_{oc} - iR_{int} \quad (1)$$

where V_{oc} and R_{int} are the open-circuit voltage (when $i = 0$) and internal resistance, respectively. Voltage suppression due to the increase in the discharge current is less severe in cell B compared to cell A, which indicates a lower R_{int} in cell B. Normalized discharge capacities (to those obtained with a 0.2C discharge rate) of cells A and B (set of four each) are listed in Table S1 and indicate a slightly lower high-rate dischargeability of cell B (average value of 84.1% in cell B vs 87.6% in cell A at a 10C rate). However, the capacities of cell B are higher than those of cell A at all discharge rates.

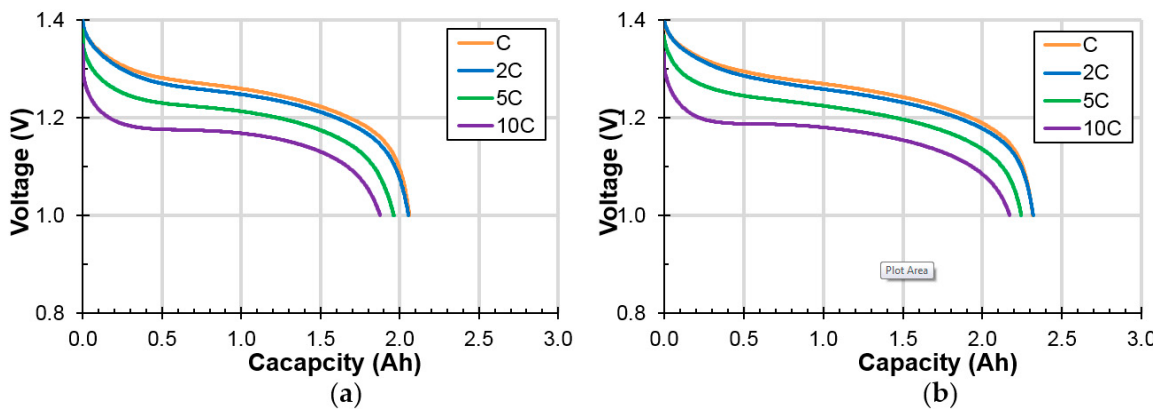


Figure 5. Discharge voltage profiles at different discharge rates of (a) cell A, and (b) cell B measured at room temperature.

3.2.2. Low Temperature

Low-temperature performances of cells A and B were evaluated by measuring the capacities at $-10\text{ }^{\circ}\text{C}$ with different discharge rates (C, 2C, 5C, and 10C). The resulting discharge voltage profiles are plotted in Figure 6. Voltage suppression due to the increase in the discharge current is more severe at a lower temperature. Only about 50% of the capacity is obtained at $-10\text{ }^{\circ}\text{C}$ with C and 2C discharge rates. The cells deliver almost no capacity with further increases in the discharge rate. Normalized $-10\text{ }^{\circ}\text{C}$ discharge capacities (to those obtained at RT with a 0.2C discharge rate) of cells A and B (set of four each) are listed and indicate a slightly better low-temperature performance of cell B (average value of 51.6% in cell B vs 49.0% in cell A at a 1C rate).

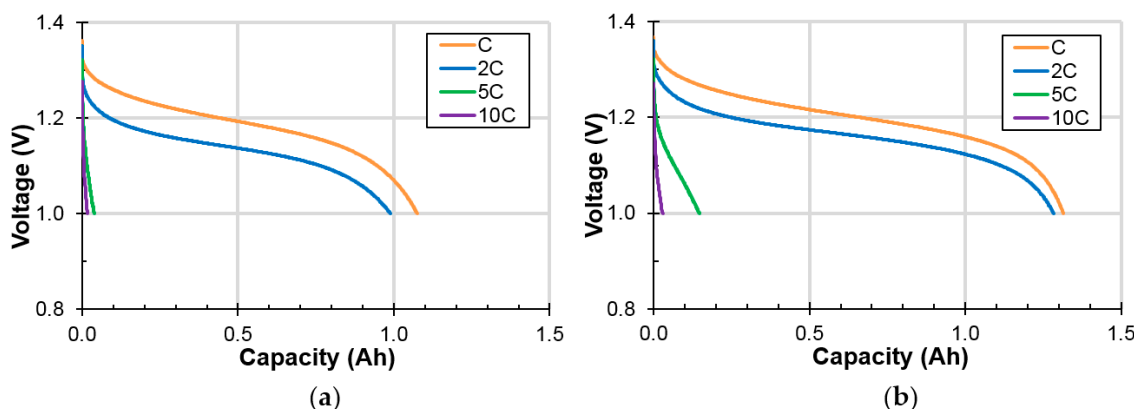


Figure 6. Discharge voltage profiles at different discharge rates of (a) cell A, and (b) cell B measured at $-10\text{ }^{\circ}\text{C}$.

3.2.3. Charge Retention

Charge-retention behaviors of cells A and B were evaluated by both the RT and $-10\text{ }^{\circ}\text{C}$ standing voltage stabilities at an 80% state-of-charge, and the results are plotted in Figures 7 and 8, respectively. On average, cell A demonstrates a marginally better charge-retention performance at RT but a worse performance at $-10\text{ }^{\circ}\text{C}$ compared to cell B.

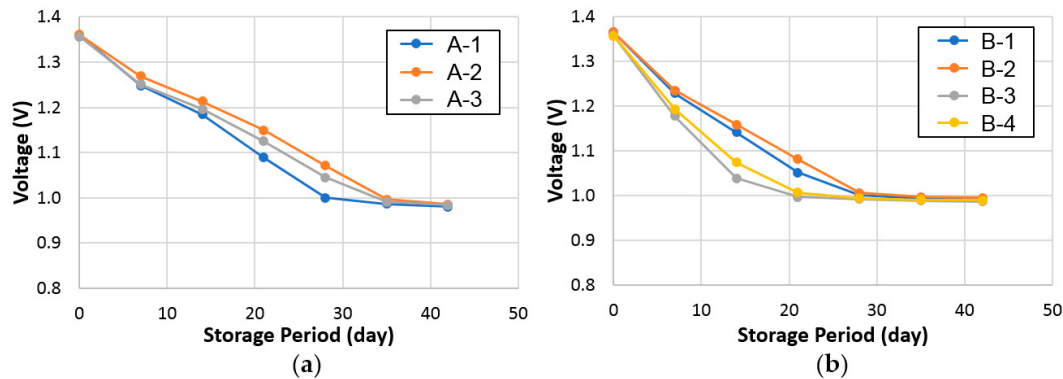


Figure 7. Open-circuit voltages of (a) cell A (set of three), and (b) cell B (set of four) stored at room temperature.

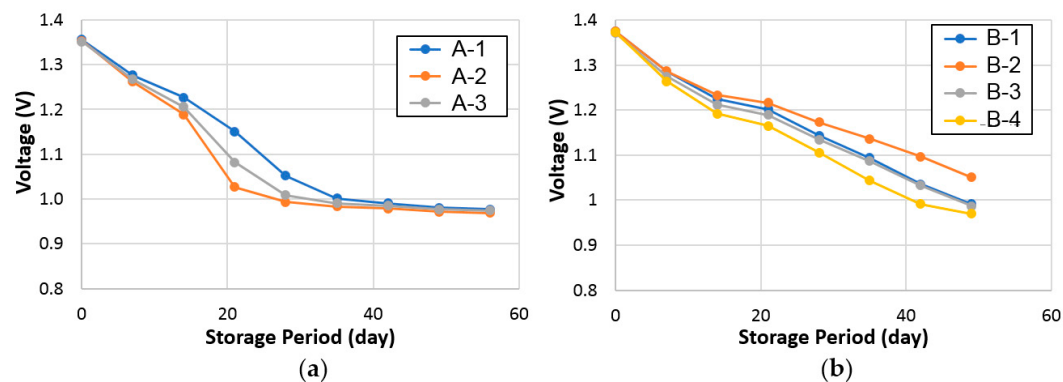


Figure 8. Open-circuit voltages of (a) cell A (set of three), and (b) cell B (set of four) stored at $-10\text{ }^{\circ}\text{C}$.

3.2.4. Internal Resistance

Internal resistance (R_{int}) was measured by a pulse method using the formula:

$$R_{\text{int}} = \Delta V / \Delta i \quad (2)$$

Both 1 and 10 s pulses were used to measure R_{int} s from cells A and B, and data obtained at both RT and $-10\text{ }^{\circ}\text{C}$ are listed in Table 4. RT R_{int} s decreases slightly with the increase in the discharge rate. Cell B shows a lower R_{int} s in all measurements.

Table 4. Internal resistances (R_{int} , in $\text{m}\Omega \cdot \text{m}^2$) measured with 1 and 10 s pulsed discharges with different discharge rates (1, 2, 5, and 10C) at both room temperature (RT) and $-10\text{ }^{\circ}\text{C}$.

Condition	1C	2C	5C	10C
Cell A RT 1 s	0.144	0.142	0.138	0.130
Cell A RT 10 s	0.194	0.192	0.182	0.168
Cell A $-10\text{ }^{\circ}\text{C}$ 1 s	0.405	0.369	0.289	0.244
Cell A $-10\text{ }^{\circ}\text{C}$ 10 s	0.516	0.492	0.499	—
Cell B RT 1 s	0.087	0.087	0.087	0.085
Cell B RT 10 s	0.127	0.127	0.124	0.118
Cell B $-10\text{ }^{\circ}\text{C}$ 1 s	0.334	0.312	0.262	0.219
Cell B $-10\text{ }^{\circ}\text{C}$ 10 s	0.468	0.444	0.453	—

3.2.5. Surface Charge-Transfer Resistance

Out of many factors contributing to R_{int} , ohmic resistance (R_0) and surface charge-transfer resistance (R_{ct}) can be deduced from the Cole-Cole plot obtained by the alternating current (AC) impedance measurement [35]. Cole-Cole plots of cells A and B measured at RT and -10°C are shown in Figures 9 and 10, respectively. Calculated R_0 and R_{ct} values, and double-layer capacitances (C) of cells A and B are listed in Table S2. While R_0 values in both sets are similar, R_{ct} values in cell B are lower than those in cell A at both RT and -10°C . Part of the reason for the lower R_{ct} values in cell B is due to the larger surface reactive area (A) of the superlattice alloy from the connection:

$$C = \epsilon A / d \quad (3)$$

where ϵ and d are the dielectric constant of electrolyte and the alloy surface dipole thickness. Another reason for the lower R_{ct} values in cell B is the higher surface catalytic ability of the superlattice alloy [28].

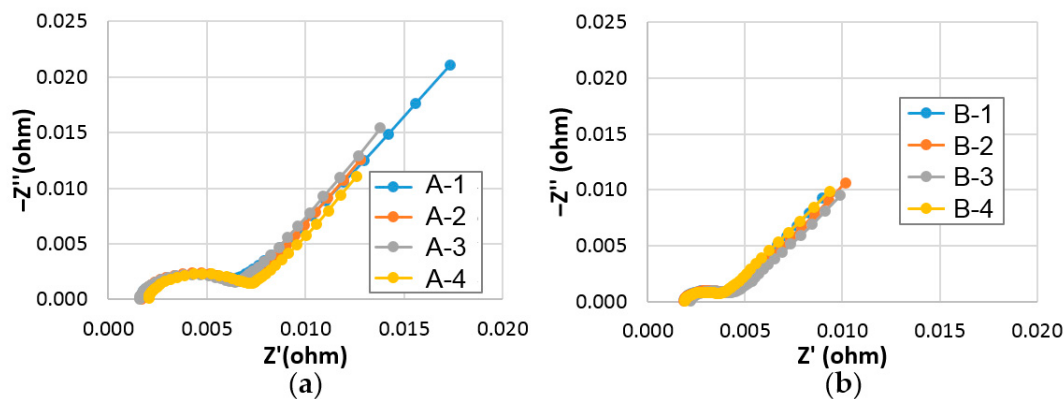


Figure 9. Cole-Cole plots of (a) cell A (set of four), and (b) cell B (set of four) measured at room temperature.

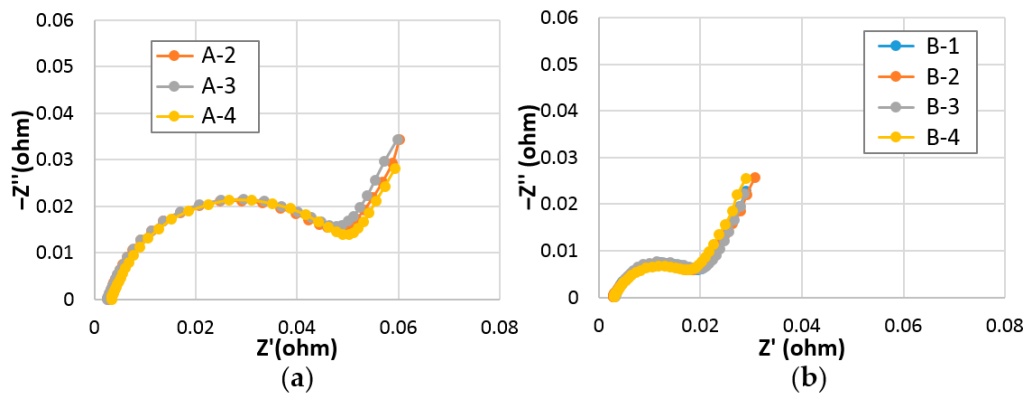


Figure 10. Cole-Cole plots of (a) cell A (set of three), and (b) cell B (set of four) measured at -10°C .

3.2.6. Cycle Life

Because the high-power design is usually associated with shallow charge/discharge cycling, a regular C-size configuration with a nominal capacity of 4.5 Ah was used to study the cycle life performance. Cells were built with annealed alloys A and B and tested under a C/2 charge to a $-\Delta V$ of 3 mV and a C/2 discharge to a cutoff voltage of 0.9 V at RT, and the results are plotted in Figure 11. Without the protective binder commonly used in the commercial cells made with the superlattice alloys [32], the cell made with the superlattice MH alloy (alloy B) only shows half of the cycle life of

a cell made with the conventional AB_5 MH alloy (alloy A). Earlier studies on the failure mode of a Mm-based Al-free superlattice MH alloy indicated that the pulverization of the main phase is the main cause of capacity degradation [30].

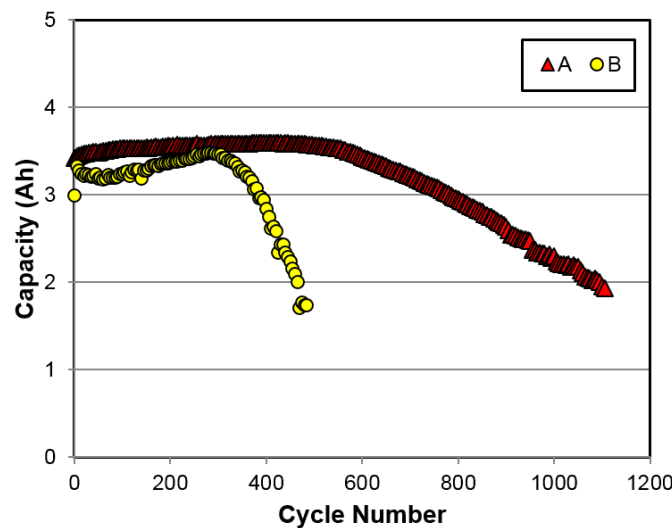


Figure 11. Room temperature cycle life (C/2-C/2) comparison between regular C-size cells (not high-power) made with annealed alloys A and B.

3.2.7. Comparison

A battery performance comparison between cells made with the AB_5 (cell A) and Al-free A_2B_7 -based superlattice (cell B) MH alloys is summarized in Figure 12. Cell B has a higher capacity and a better low-temperature performance; however, it demonstrates slightly worse high-rate dischargeability and charge retention, and its cycle life is only half that of cell A. Despite the lower R_{int} and R_{ct} in cell B, it still shows a lower normalized capacity at a higher rate, which may be associated with the relatively low V_{oc} at RT caused by alloy B's relatively low equilibrium plateau pressure (Figure 2). In another article, cells made with an Al-containing superlattice MH alloy showed a comparable cycle life and better peak power and charge-retention performance compared to those made with the AB_5 alloy [19]. Therefore, the inferior cycle life observed in the superlattice alloy is only limited to the Al-free composition used in this study. Combined with the use of a hydrophobic binder in the negative-electrode paste [32], the Al-containing superlattice alloy showed even better cycle stability [8].

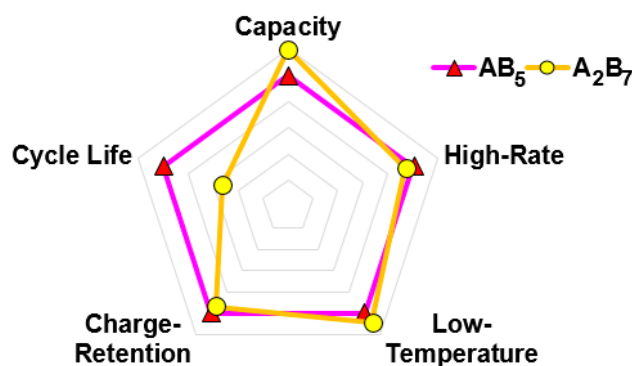


Figure 12. Sealed-cell performance comparison between cells made with the conventional AB_5 and new A_2B_7 -based superlattice MH alloys.

4. Conclusions

Electrochemical performances of a misch metal-based Al-free superlattice metal hydride alloy were compared to those of a standard AB₅ metal hydride alloy in a high-power C-size cell configuration. In the sealed cell, the superlattice alloy showed higher energy densities, lower internal resistances, lower surface charge-transfer resistances at both RT and –10 °C compared to the AB₅ alloy. For the charge-retention performance, the superlattice alloy was slightly worse at RT but outperformed the AB₅ alloy at –10 °C. The cycle stability of the superlattice alloy tested in a regular cell configuration is inferior to that of the AB₅ alloy mainly because of alloy pulverization.

Supplementary Materials: The following are available online at <http://www.mdpi.com/2313-0105/3/4/35/s1>, Table S1: Discharge capacities normalized to those obtained at a 0.2C rate from four Cells A and four Cells B measured at both room temperature and –10 °C. All numbers are in %. SD denotes standard deviation, Table S2: Ohmic resistances (R₀ in W), surface charge-transfer resistances (R_{ct} in W), and double-layer capacitances (C in Farad) from Cells A and B measured at both room temperature (RT) and –10 °C. SD denotes standard deviation.

Acknowledgments: The authors would like to thank the following individuals from BASF—Ovonic for their help: Su Cronogue, Taihei Ouchi, Jean Nei, Shiuan Chang, Nathan English, Sui-ling Chen, Cheryl Setterington, David Pawlik, Allen Chan, and Ryan J. Blankenship.

Author Contributions: John M. Koch designed and performed the experiments. Kwo-Hsiung Young prepared the alloys and the manuscript. Chaolan Hu and Benjamin Reichman conducted the AC impedance measurements and interpreted the data.

Conflicts of Interest: The authors declare no conflict of interest.

Abbreviations

Ni/MH	Nickel/metal hydride
Mm	Misch metal
MH	Metal hydride
RE	Rare-earth
XRD	X-ray diffractometer
SEM	Scanning electron microscope
PCT	Pressure-concentration-temperature
EDS	Energy-dispersive spectroscopy
HEX	Hexagonal
CUB	Cubic
RHO	Rhombohedral
Abs	Absorption
Des	Desorption
RT	Room temperature
V	Cell voltage
i	Current
V _{oc}	Open-circuit voltage
R _{int}	Internal resistance
R ₀	Ohmic resistance
R _{ct}	Charge-transfer resistance
C	Double-layer capacitance
A	Surface reactive area
ε	Dielectric constant of electrolyte
d	Alloy surface dipole thickness

References

1. Zelinsky, M.A.; Koch, J.M.; Young, K. Performance comparison of rechargeable batteries for stationary applications (Ni/MH vs. Ni-Cd and VRLA). *Batteries* **2017**, submitted.
2. Young, K.; Cai, X.; Chang, S. Reviews on Chinese Patents regarding the nickel/metal hydride battery. *Batteries* **2017**, *3*, 24. [CrossRef]

3. Yasuoka, S.; Magari, Y.; Murata, T.; Tanaka, T.; Ishida, J.; Nakamura, H.; Nohma, T.; Kihara, M.; Baba, Y.; Teraoka, H. Development of high-capacity nickel-metal hydride batteries using superlattice hydrogen-absorbing alloys. *J. Power Sour.* **2006**, *156*, 662–666. [[CrossRef](#)]
4. Teraoka, H. Development of Low Self-Discharge Nickel-Metal Hydride Battery. Available online: <http://www.scribd.com/doc/9704685/Teraoka-Article-En> (accessed on 9 April 2016).
5. Kai, T.; Ishida, J.; Yasuoka, S.; Takeno, K. The effect of nickel-metal hydride battery's characteristics with structure of the alloy. In Proceedings of the 54th Battery Symposium in Japan, Osaka, Japan, 6–9 October 2013; p. 210.
6. Teraoka, H. Development of Ni-MH EThSS with Lifetime and Performance Estimation Technology. In Proceedings of the 34th International Battery Seminar & Exhibit, Fort Lauderdale, FL, USA, 20–23 March 2017.
7. Teraoka, H. Ni-MH Stationary Energy Storage: Extreme Temperature & Long Life Developments. In Proceedings of the 33th International Battery Seminar & Exhibit, Fort Lauderdale, FL, USA, 21–24 March 2016.
8. Teraoka, H. Development of Highly Durable and Long Life Ni-MH Batteries for Energy Storage Systems. In Proceedings of the 32th International Battery Seminar & Exhibit, Fort Lauderdale, FL, USA, 9–12 March 2015.
9. Liu, Y.; Cao, Y.; Huang, L.; Gao, M.; Pan, H. Rare earth-Mg-Ni-based hydrogen storage alloys as negative electrode materials for Ni/MH batteries. *J. Alloy. Compd.* **2011**, *509*, 675–686. [[CrossRef](#)]
10. Young, K.; Nei, J. The current status of hydrogen storage alloy development for electrochemical applications. *Materials* **2013**, *6*, 4574–4608. [[CrossRef](#)] [[PubMed](#)]
11. Liu, J.; Han, S.; Li, Y.; Zhang, L.; Zhao, Y.; Yang, S.; Liu, B. Phase structures and electrochemical properties of La–Mg–Ni-based hydrogen storage alloys with superlattice structure. *Int. J. Hydrogen Energy* **2016**, *41*, 20261–20275. [[CrossRef](#)]
12. Takasaki, T.; Nishimura, K.; Saito, M.; Fukunaga, H.; Iwaki, T.; Sakai, T. Cobalt-free nickel-metal hydride battery for industrial applications. *J. Alloy. Compd.* **2013**, *580*, S378–S381. [[CrossRef](#)]
13. Yasuoka, S.; Ishida, J.; Kai, T.; Kajiwara, T.; Doi, S.; Yamazaki, T.; Kishida, K.; Inui, H. Function of aluminum in crystal structure of rare earth-Mg-Ni hydrogen-absorbing alloy and deterioration mechanism of Nd_{0.9}Mg_{0.1}Ni_{3.4} and Nd_{0.9}Mg_{0.1}Ni_{3.3}Al_{0.2} alloys. *Int. J. Hydrogen Energy* **2017**, *42*, 11574–11583. [[CrossRef](#)]
14. Young, K.; Wong, D.F.; Wang, L.; Nei, J.; Ouchi, T.; Yasuoka, S. Mn in misch-metal based superlattice metal hydride alloy—Part 1 Structural, hydrogen storage and electrochemical properties. *J. Power Sour.* **2015**, *277*, 426–432. [[CrossRef](#)]
15. Young, K.; Wong, D.F.; Wang, L.; Nei, J.; Ouchi, T.; Yasuoka, S. Mn in misch-metal based superlattice metal hydride alloy—Part 2 Ni/MH battery performance and failure mechanism. *J. Power Sour.* **2015**, *277*, 433–442. [[CrossRef](#)]
16. Young, K.; Ouchi, T.; Nei, J.; Yasuoka, S. Fe-substitution for Ni in misch metal-based superlattice hydrogen absorbing alloys—Part 1. Structural, hydrogen storage, and electrochemical properties. *Batteries* **2016**, *2*, 34. [[CrossRef](#)]
17. Meng, T.; Young, K.; Nei, J.; Koch, J.M.; Yasuoka, S. Fe-substitution for Ni in misch metal-based superlattice hydrogen absorbing alloys—Part 2. Ni/MH battery performance and failure mechanisms. *Batteries* **2017**, *3*, 28. [[CrossRef](#)]
18. Wang, L.; Young, K.; Meng, T.; Ouchi, T.; Yasuoka, S. Partial substitution of cobalt for nickel in mixed rare earth metal based superlattice hydrogen absorbing alloy—Part 1 structural, hydrogen storage and electrochemical properties. *J. Alloy. Compd.* **2016**, *660*, 407–415. [[CrossRef](#)]
19. Wang, L.; Young, K.; Meng, T.; English, N.; Yasuoka, S. Partial substitution of cobalt for nickel in mixed rare earth metal based superlattice hydrogen absorbing alloy—Part 2 battery performance and failure mechanism. *J. Alloy. Compd.* **2016**, *664*, 417–427. [[CrossRef](#)]
20. Meng, T.; Young, K.; Koch, J.; Ouchi, T.; Yasuoka, S. Failure mechanisms of nickel/metal hydride batteries with cobalt-substituted superlattice hydrogen-absorbing alloy anodes at 50 °C. *Batteries* **2016**, *2*, 20. [[CrossRef](#)]
21. Yasuoka, S.; Ishida, J.; Kishida, K.; Inui, H. Effects of cerium on the hydrogen absorption-desorption properties of rare earth-Mg-Ni hydrogen-absorbing alloys. *J. Power Sour.* **2017**, *346*, 56–62. [[CrossRef](#)]
22. Young, K.; Chang, S.; Lin, X. C14 Laves phase metal hydride alloys for Ni/MH batteries applications. *Batteries* **2017**, *3*, 27. [[CrossRef](#)]

23. Chang, S.; Young, K.; Nei, J.; Fierro, C. Reviews on the U.S. Patents regarding nickel/metal hydride batteries. *Batteries* **2016**, *2*, 10. [[CrossRef](#)]
24. Young, K.; Wang, L.; Yan, S.; Liao, X.; Meng, T.; Shen, H.; May, W.C. Fabrications of high-capacity alpha-Ni(OH)₂. *Batteries* **2017**, *3*, 6. [[CrossRef](#)]
25. Young, K.; Wu, A.; Qiu, Z.; Tan, J.; Mays, W. Effects of H₂O₂ addition to the cell balance and self-discharge of Ni/MH batteries with AB₅ and A₂B₇ alloys. *Int. J. Hydrogen Energy* **2012**, *37*, 9882–9891. [[CrossRef](#)]
26. Young, K.; Koch, J.M.; Wan, C.; Denys, R.V.; Yartys, V.A. Cell performance comparison between C14- and C15-predominated AB₂ metal hydride alloys. *Batteries* **2017**, *3*, 29. [[CrossRef](#)]
27. Yan, S.; Meng, T.; Young, K.; Nei, J. A Ni/MH pouch cell with high-capacity Ni(OH)₂. *Tatteries* **2017**, submitted.
28. Meng, T.; Young, K.; Hu, C.; Reichman, B. Effects of alkaline pre-etching to metal hydride alloys. *Batteries* **2017**, *3*, 30. [[CrossRef](#)]
29. Young, K.; Ouchi, T.; Koch, J.M.; Lien, Y. Comparison among constituent phases in superlattice metal hydride alloys for battery applications. *Tatteries* **2017**, submitted. [[CrossRef](#)]
30. Zhou, X.; Young, K.; West, J.; Regalado, J.; Cherisol, K. Degradation mechanisms of high-energy bipolar nickel metal hydride battery with AB₅ and A₂B₇ alloys. *J. Alloy. Compd.* **2013**, *580*, S373–S377. [[CrossRef](#)]
31. Young, K.; Ouchi, T.; Huang, B. Effects of various annealing conditions on (Nd, Mg, Zr)(Ni, Al, Co)_{3.74} metal hydride alloys. *J. Power Sour.* **2014**, *248*, 147–153. [[CrossRef](#)]
32. Ouchi, T.; Young, K.; Moghe, D. Reviews on the Japanese Patent Applications regarding nickel/metal hydride batteries. *Batteries* **2016**, *2*, 21. [[CrossRef](#)]
33. Young, K.; Ouchi, T.; Meng, T.; Wong, D.F. Studies on the synergetic effects in multi-phase metal hydride alloys. *Batteries* **2016**, *2*, 15. [[CrossRef](#)]
34. Osumi, Y. *Suiso Kyuzou Goukin*; Agune Technology Center: Tokyo, Japan, 1999; p. 218. (In Japanese)
35. Zhang, L. AC impedance studies on sealed nickel metal hydride batteries over cycle life in analog and digital operations. *Electrochim. Acta* **1998**, *43*, 3333–3342. [[CrossRef](#)]



© 2017 by the authors. Licensee MDPI, Basel, Switzerland. This article is an open access article distributed under the terms and conditions of the Creative Commons Attribution (CC BY) license (<http://creativecommons.org/licenses/by/4.0/>).